第 43 卷 第 20 期/2023 年 10 月/光学学报 研究论文

光学学报

银纳米颗粒复合非晶氧化镓光电探测器的制备与研究

许强，杨莉莉**，刘增，张茂林，李山，唐为华*

南京邮电大学集成电路科学与工程学院，江苏 南京 210023

摘要 氧化镓(Ga_2O_3)因其合适的禁带宽度(4.5～5.3 eV)在深紫外探测方面具有天然的优势。本文利用常温磁控溅射技术在非晶Ga_2O_3薄膜表面溅射银纳米颗粒，制备出简易的深紫外光电探测器。结果表明，在5 V偏压下，探测器的暗电流低至94 fA，光暗电流比高达5.9×10^5，254 nm/365 nm波长抑制比达到1.6×10^4，探测率为2×10^{14} Jones(探测率单位)，且该探测器在不同电压和不同光强下都能快速且稳定地响应。该探测器优异的深紫外光探测表现与引入的金属银纳米颗粒密切相关。一方面，银纳米颗粒与Ga_2O_3薄膜间的肖特基势垒的形成有助于减小非晶Ga_2O_3的暗电流；另一方面，银纳米颗粒的表面等离子振动有助于增强Ga_2O_3对紫外光的吸收，且紫外光照下银纳米颗粒会产生大量的热载流子使得热电子有足够的能量克服银纳米颗粒与Ga_2O_3薄膜间的肖特基势垒，使得探测器的光电流增加。本文工作为实现具有低暗电流和高光暗电流比的深紫外光电探测器提供了一种可行的方法。

关键词 光电探测器；氧化镓；银纳米颗粒；热电子；肖特基势垒

中图分类号 TM23 **文献标志码** A **DOI**：10.3788/AOS230813

1 引 言

大气层中的臭氧层等对波长低于280 nm的深紫外(DUV)光具有强烈的吸收和散射作用，使得进入到地球大气层内的太阳辐射中深紫外光几乎为零。干净的背景噪声赋予了深紫外光电探测较低的误警率和较高的信噪比等优点，使得其受到越来越多的学者的关注，并在臭氧空洞探测、高压电火灾报警、隐形轰炸机和导弹报警方面具有很大的应用潜力[1-2]。深紫外光电探器主要采用宽禁带半导体材料，常见的包括AlGaN[3-4]、MgZnO[5-6]、金刚石[7]、氧化镓(Ga_2O_3)[8]等。其中，Ga_2O_3作为一种新型的光电材料，无须进行合金化过程，制备简单、稳定性高，且Ga_2O_3具有适合深紫外波段探测的可调的能带带隙(4.5～5.3 eV)，是制备深紫外光电探测器最理想的材料之一[9]。Ga_2O_3共有五种同分异构体，分别为α-Ga_2O_3、β-Ga_2O_3、ε-Ga_2O_3、δ-Ga_2O_3和γ-Ga_2O_3，其中最稳定的为β相Ga_2O_3[10]。目前很多研究都集中在结晶相的Ga_2O_3薄膜上，但是高质量的晶体薄膜在制备过程中容易受到衬底的晶格匹配和严格的生长参数的影响，从而对衬底材料和薄膜生长设备均提出了较高的要求，因此Ga_2O_3晶体薄膜往往具有制备成本高、重现性差等缺点。

非晶Ga_2O_3薄膜一般采用磁控溅射、脉冲激光沉积等技术，制备过程简单、成本低廉[11]。相较于结晶Ga_2O_3，非晶Ga_2O_3含有更高密度的氧空位等缺陷，这些缺陷一方面有助于捕获光生载流子，促进电荷分离；另一方面又可以作为光生载流子的复合中心，降低电荷分离效率[12]，因此非晶Ga_2O_3更容易在深紫外光的激发下展现出大的光电流。综上这些优点使得非晶Ga_2O_3薄膜在紫外光电器件材料中受到关注。但非晶Ga_2O_3薄膜由于其较差的结晶性，往往器件的暗电流也较高。贵金属纳米颗粒如Au、Ag、Cu等[13]具有固有的等离子振动频率，紫外光下的贵金属表面等离子振动可以增强对入射光的散射作用，从而有利于提高探测器对入射光的吸收和探测[14]。且紫外光照下贵金属纳米颗粒会产生大量的热载流子，使得热电子有足够的能量克服Ag纳米颗粒与Ga_2O_3薄膜间的肖特基势垒，从而增加探测器的光电流。此外，具有合适功函数的金属的引入还有助于在半导体-金属界面形成势垒区，使得暗电流进一步降低。因此，为了进一步提高非晶Ga_2O_3基光电探测器对深紫外信号的探测灵敏度，向非晶Ga_2O_3薄膜表面引入贵金属纳米颗粒是一种可行的实现方式。目前已有许多报道通过引入贵金属颗粒来提高探测器的性能。如石雄林等[15]利用快速

收稿日期：2023-04-13；**修回日期**：2023-05-18；**录用日期**：2023-05-31；**网络首发日期**：2023-06-28

基金项目：国家重点研发计划(2022YFB3605400)、国家自然科学基金(62204125，62204126)、南京邮电大学引进人才科研启动基金(自然科学)(NY221119，NY221115，NY221002)

通信作者：*whtang@njupt.edu.cn；**liliyang@njupt.edu.cn

热退火的方法在β-Ga_2O_3薄膜表面形成了直径为12～40 nm的铝纳米颗粒(Al-NPs)，并成功制备了Al-NPs/β-Ga_2O_3日盲紫外探测器。Al纳米颗粒的存在不仅降低了探测器件的暗电流，同时也增大了探测器件的光响应度和探测率。除此之外，铝纳米颗粒增加了β-Ga_2O_3薄膜对入射光的散射，且铝纳米颗粒周围电磁场的增强促使了器件的内部增益变大，从而使器件光响应度和探测率增大。10 V偏压下，Al-NPs/β-Ga_2O_3探测器的光响应度达到了2.7 A/W，探测率达到了1.35×10^{14} cm·$Hz^{1/2}$·W^{-1}，另外，Al-NPs/β-Ga_2O_3探测器的衰减率(10^3)得到大幅提高。An等[16]通过在β-Ga_2O_3薄膜上沉积Au纳米颗粒(Au-NPs)制备复合薄膜，然后进行后热处理。与β-Ga_2O_3薄膜相比，在Au-NPs/β-Ga_2O_3的紫外-可见光谱中观察到510 nm附近有显著的吸收。结果表明，Au-NPs/β-Ga_2O_3的光响应在254 nm+532 nm光照射下的光电探测器远高于在254 nm光照射下的光电探测器，同时由表面等离子激元效应辅助的β-Ga_2O_3薄膜光电探测器具有高鲁棒性和良好的可重复性，能够表现出相对较快的响应速度和恢复速度，表明在Ga_2O_3表面引入金属纳米颗粒可有效改善光电探测器的性能。

银(Ag)作为一种贵金属材料，其固有的等离子振动吸收峰位于400 nm附近，且Ag纳米颗粒具有合适的功函数(4.6 eV)[17]，能够与非晶Ga_2O_3薄膜形成肖特基接触界面。因此，本文旨在利用金属Ag纳米颗粒复合Ga_2O_3薄膜(Ag-NPs/Ga_2O_3)来提高探测器的光电流并降低其暗电流。具体操作是采用常温射频磁控溅射技术在蓝宝石衬底表面溅射一层Ga_2O_3薄膜，再通过直流磁控溅射技术将Ag纳米颗粒溅射到Ga_2O_3薄膜表面形成复合薄膜。基于Ag-NPs/Ga_2O_3得到的光电探测器表现出优异的深紫外探测性能，在5 V偏压下，探测器的暗电流低至94 fA，光暗电流比高达5.9×10^5，254 nm/365 nm波长抑制比达到1.6×10^4，其响应度为36.1 mA/W，探测率为2×10^{14} Jones(探测率单位)，外量子效率为17.7%，较相应的Ga_2O_3基光电探测器均得到了较大的提升。

2 实验方法

本文采用射频磁控溅射技术在(0001)面的蓝宝石衬底上生长Ga_2O_3薄膜。溅射在常温下进行，溅射时的腔室气压和所通的氩气流量分别为1 Pa和20 sccm，溅射总时间为70 min。溅射完毕后将所得到的Ga_2O_3薄膜切成4份，取其中3份采用直流磁控溅射技术继续在Ga_2O_3表面溅射Ag纳米颗粒，溅射时间分别为5、10、20 s，获得的样品分别标记为5 s Ag-NPs/Ga_2O_3、10 s Ag-NPs/Ga_2O_3、20 s Ag-NPs/Ga_2O_3[18]。最后，将上述得到的4份样品放入管式炉中退火2 h，退火温度为200 ℃。用X射线衍射仪(XRD)对样品的晶体结构进行表征，用扫描电子显微镜(SEM)对所得样品断面形貌进行表征，用原子力显微镜(AFM)对所得样品表面形貌进行表征，用上海元析Q6紫外-可见(UV-Vis)分光光度计对样品的光谱吸收进行表征，采用波长分别为254 nm和365 nm的低压汞灯作为紫外光光源。在样品表面压上直径为1 mm、间距为1 mm的圆柱形金属铟作为电极，并使用B1505A功率器件分析仪测量Ag-NPs/Ga_2O_3薄膜光电探测器的电流-电压(I-V)特性和瞬态响应(I-t)特性[19-20]。

3 分析与讨论

图1(a)为Ga_2O_3薄膜断面的SEM图，图中显示在蓝宝石表面生长了一层Ga_2O_3薄膜，膜厚约为138 nm。图1(b)为20 s Ag-NPs/Ga_2O_3薄膜的XRD图，从图中可以看出，除了在41°～42°处存在蓝宝石衬底的衍射峰外，没有其他明显的衍射峰，这表明制备的20 s Ag-NPs/Ga_2O_3薄膜为非晶态[21]。图1(c)和1(d)分别为Ga_2O_3和20 s Ag-NPs/Ga_2O_3薄膜的AFM图，与图1(c)相比，图1(d)中存在明显的较为突出的区域，平均高度约为25.8 nm，这可能是Ag纳米颗粒的存在使得20 s Ag-NPs/Ga_2O_3薄膜样品表面均方根粗糙度(RMS)远高于Ga_2O_3薄膜[图1(c)、1(d)的RMS分别为0.218、6.390 nm]。图1(e)为非晶Ga_2O_3和不同溅射条件下的Ag-NPs/Ga_2O_3薄膜的吸收光谱图，从图中可以看出，非晶Ga_2O_3仅在波长194 nm处有一个明显的吸收峰。随着溅射Ag时间的增加，在450 nm左右也逐渐出现了一个较宽的吸收峰。该吸收峰的产生主要来自于Ag纳米颗粒在450 nm处的等离子振动，该等离子振动峰的出现证实了Ag纳米颗粒的形成以及其已被成功复合在非晶Ga_2O_3薄膜的表面。此外，值得注意的是，溅射Ag纳米颗粒的三个样品上来自于Ga_2O_3的吸收峰位置均出现了轻微的红移，且对紫外光吸收均有所增强，表明Ag纳米颗粒的引入对Ga_2O_3薄膜表面的紫外光吸收产生了影响。图1(f)是根据图1(e)所绘制的$(\alpha h\nu)^2$-$h\nu$曲线图，对于Ga_2O_3而言，其光学带隙与吸收系数之间满足Tauc关系式，表达式为

$$(\alpha h\nu)^2 = A^2(h\nu - E_g), \tag{1}$$

式中：α为吸收系数；$h\nu$为入射光子能；A^2表示吸收边的斜率；E_g为光学带隙。从图中可以看出，其Ga_2O_3、5 s Ag-NPs/Ga_2O_3、10 s Ag-NPs/Ga_2O_3、20 s Ag-NPs/Ga_2O_3的光学带隙分别为5.16、4.98、4.98、5.09 eV左右，与所报道的Ga_2O_3相近[22]，这为制备高性能的光电探测器提供了保证。此外，Ag-NPs/Ga_2O_3薄膜较非晶Ga_2O_3薄膜表现出更低的光学带隙，这是由于Ag纳米颗粒增强了Ga_2O_3薄膜对紫外光的吸收，使得Ag-NPs/Ga_2O_3薄膜的吸光度高于非晶Ga_2O_3薄膜，且吸收带边略有红移，根据Tauc关系式，Ag-NPs/Ga_2O_3薄膜的光学带隙低于非晶Ga_2O_3薄膜。

图2(a)显示了非晶Ga_2O_3和20 s Ag-NPs/Ga_2O_3薄膜光电探测器在黑暗情况下的I-V曲线。对暗电流

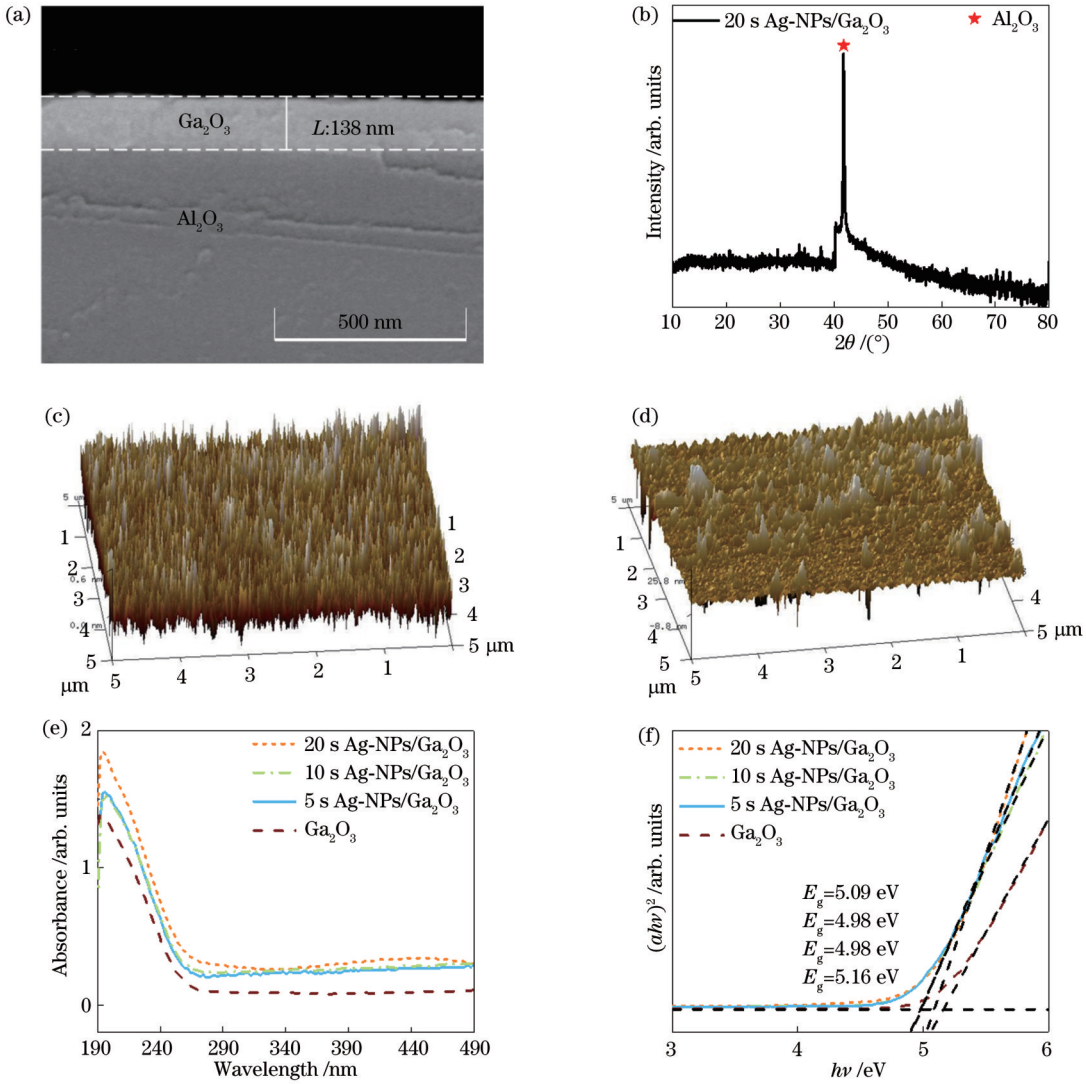

图 1 Ga_2O_3薄膜材料表征。(a)蓝宝石衬底上常温生长的Ga_2O_3薄膜断面SEM图像；(b)20 s Ag-NPs/Ga_2O_3的XRD图；(c)Ga_2O_3的AFM图像；(d)20 s Ag-NPs/Ga_2O_3的AFM图像；(e)Ga_2O_3和Ag-NPs/Ga_2O_3的吸收光谱图；(f)$(\alpha h\nu)^2$-$h\nu$曲线图

Fig. 1 Material characterization of Ga_2O_3 film. (a) SEM image of cross section of Ga_2O_3 film grown on sapphire substrate at room temperature; (b) XRD image of 20 s Ag-NPs/Ga_2O_3; (c) AFM image of Ga_2O_3; (d) AFM image of 20 s Ag-NPs/Ga_2O_3; (e) absorption spectra of Ga_2O_3 and Ag-NPs/Ga_2O_3; (f) curve of $(\alpha h\nu)^2$-$h\nu$

曲线进行拟合可以看出，在−5～5 V之间，非晶Ga_2O_3光电探测器的暗电流明显大于20 s Ag-NPs/Ga_2O_3光电探测器的暗电流。在5 V偏压下，非晶Ga_2O_3光电探测器的暗电流为148 fA，经过Ag纳米颗粒复合后，20 s Ag-NPs/Ga_2O_3光电探测器的暗电流减小为94 fA，约为非晶Ga_2O_3光电探测器的2/3，达到了设备的测试极限。超低的暗电流得益于Ag纳米颗粒和Ga_2O_3薄膜之间形成的肖特基结，在二者界面处存在肖特基势垒，使得载流子越过势垒所需的能量增加，从而导致暗电流降低。图2(b)显示了非晶Ga_2O_3、5 s Ag-NPs/Ga_2O_3、10 s Ag-NPs/Ga_2O_3和20 s Ag-NPs/Ga_2O_3薄膜光电探测器在254 nm紫外光照射下的I-V曲线。从图中可以看出，所有的I-V特性曲线均为直线，这表明薄膜与In电极之间表现为欧姆接触[23]。在相同的电压下，随着Ag纳米颗粒溅射时间的延长，对应光电探测器产生的光电流显著增大。尤其是20 s Ag-NPs/Ga_2O_3光电探测器，在施加5 V偏压的条件下，其光电流达到30 nA，分别是Ga_2O_3(1.6 nA)、5 s Ag-NPs/Ga_2O_3 (4.3 nA) 和 10 s Ag-NPs/Ga_2O_3 (6.5 nA)探测器光电流的18.8、3.9和3.1倍。这可能是由于紫外光照射下Ga_2O_3薄膜表面的Ag纳米颗粒发生等离子振动增强了对紫外光的散射，使得Ga_2O_3对紫外光的吸收增强，从而导致Ag-NPs/Ga_2O_3光电探测器光电流增加。此外，Ag纳米颗粒的振动可能会产生大量的热载流子，这会让热电子有足够的能量越过Ag纳米颗粒与Ga_2O_3薄膜间的肖特基势垒，使得探测器的光电流增加。图2(c)显示了20 s Ag-NPs/Ga_2O_3薄膜光电探测器分别在无光照、254 nm和365 nm光照下的I-V特性曲线。从图中可以看出，在254 nm光照射下，探测器在5 V的时候其光电流在

30 nA 左右，光暗电流比达到 5.9×10^5。在 365 nm 光照射下，探测器在 5 V 处有较低的光电流，为 1.9 pA，此时抑制比达到 1.6×10^4，说明得到的 20 s Ag-NPs/Ga_2O_3薄膜光电探测器有着良好的光谱选择性。值得注意的是，365 nm 紫外光照下 *I-V* 曲线出现了明显的零漂移，大约为 1.8 V。相似的情况也在很多文献中有过报道，该漂移主要发生在 365 nm 的紫外光照射条件下[24]。这主要是探测器被紫外光照射时可移动的离子漂移感应电流所导致的偏移。在 365 nm 紫外光下产生的光生电流较弱，此时可移动离子漂移诱导电流无法忽视。而当探测器被 254 nm 紫外光照射时，由于更多的光生载流子以及更大的光电流，故能将离子漂移感应电流掩盖。图 2(d)显示了 20 s Ag-NPs/Ga_2O_3薄膜光电探测器光电流随光强的变化曲线。因为光电流与光强呈非线性关系，所以用幂次定律进一步研究其数值关系，表达式为

$$I_{\text{photo}} \propto P^{\theta}, \tag{2}$$

通过拟合，θ(拟合幂数)值为 0.56。

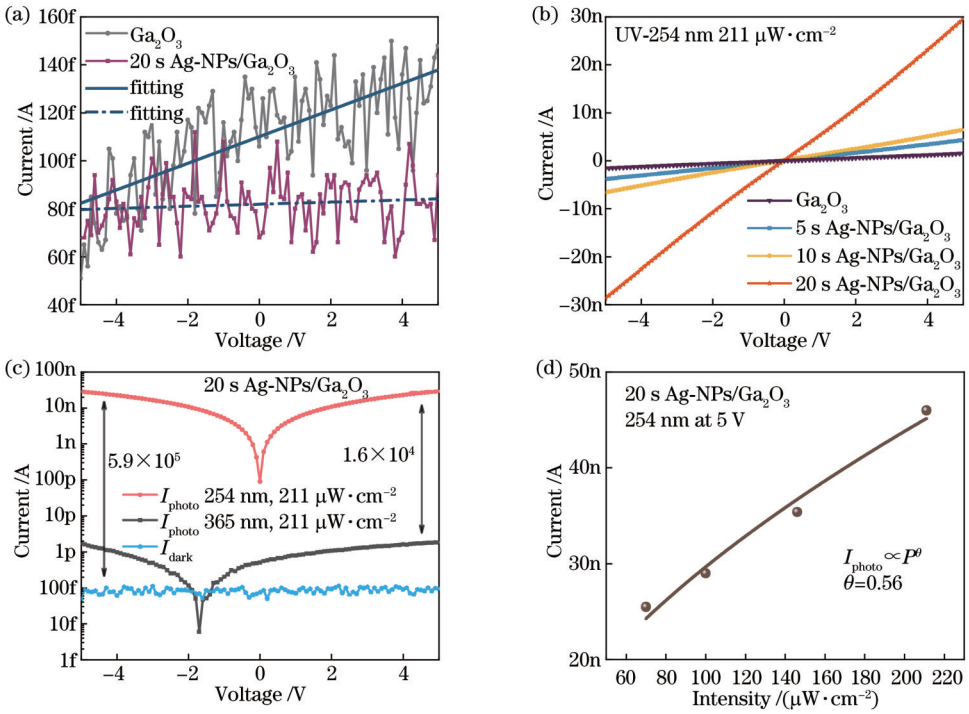

图 2 Ga_2O_3光电探测器的 *I-V* 特性曲线图。(a)在黑暗下非晶 Ga_2O_3和 Ag-NPs/Ga_2O_3薄膜光电探测器的 *I-V* 特性曲线；(b)在 254 nm 紫外光照射下非晶 Ga_2O_3和 Ag-NPs/Ga_2O_3薄膜光电探测器的 *I-V* 特性曲线；(c)20 s Ag-NPs/Ga_2O_3薄膜光电探测器分别在无光照、254 nm 和 365 nm 光照下的 *I-V* 特性曲线；(d)光电流随光强变化的曲线拟合

Fig. 2 *I-V* curves of Ga_2O_3 photodetectors. (a) *I-V* curves of amorphous Ga_2O_3 and Ag-NPs/Ga_2O_3 thin film photodetectors in dark; (b) *I-V* curves of amorphous Ga_2O_3 and Ag-NPs/Ga_2O_3 thin film photodetectors irradiated by 254 nm ultraviolet (UV) light; (c) *I-V* curves of 20 s Ag-NPs/Ga_2O_3 thin film photodetector under dark, 254 nm, and 365 nm UV lights, respectively; (d) fitted relation curve of photocurrent with light intensity

图 3(a)显示了 20 s Ag-NPs/Ga_2O_3薄膜光电探测器在 5 V 偏压下不同光强的 *I-t* 曲线。这是通过每 5 s 周期性地开关 254 nm 紫外灯来测试该探测器在不同光强下的稳定性和光依赖性能[25]。结果表明，该探测器在不同光强下都能快速响应且稳定工作，并且光强越高，工作性能越稳定。图 3(b)为 20 s Ag-NPs/Ga_2O_3薄膜探测器在光强为 211 μW/cm^2时不同偏压的 *I-t* 曲线。在 254 nm 紫外光的照射下可以看到，在不同偏压下探测器均能作出快速的响应。

本文进一步研究了在不同光强下的 Ag-NPs/Ga_2O_3薄膜探测器的性能，如图 3(a)所示，随着光强从 70 μW/cm^2增加到 211 μW/cm^2，可以看到光暗电流比(PDCR)从 2.7×10^5上升到 4.9×10^5。这是由于暗电流基本不变的情况下，光照强度越高，光电流也越高，从而光暗电流比也越高。通常探测器的光响应度用 *R* 来表示，它是检测探测器光电转换能力的重要指标，具体表达为单位入射光功率作用到探测器后在外电路中能够输出的光电流的大小，其定义式[26]为

$$R=\frac{I_{\text{photo}}-I_{\text{dark}}}{P_{\text{light}}*S}, \tag{3}$$

式中：I_{photo}、I_{dark}分别为光、暗电流；P_{light}为入射光光强；*S* 为有效照明面积。当入射光光强为 70 μW/cm^2、偏压为 5 V 时，20 s Ag-NPs/Ga_2O_3薄膜光电探测器的光响应度 *R* 为 36.1 mA/W。但是该探测器的光响应度反而随光强的增加从 36.1 mA/W 下降到 20.8 mA/W，这种现象也常见于许多其他的探测器中，这是由于探

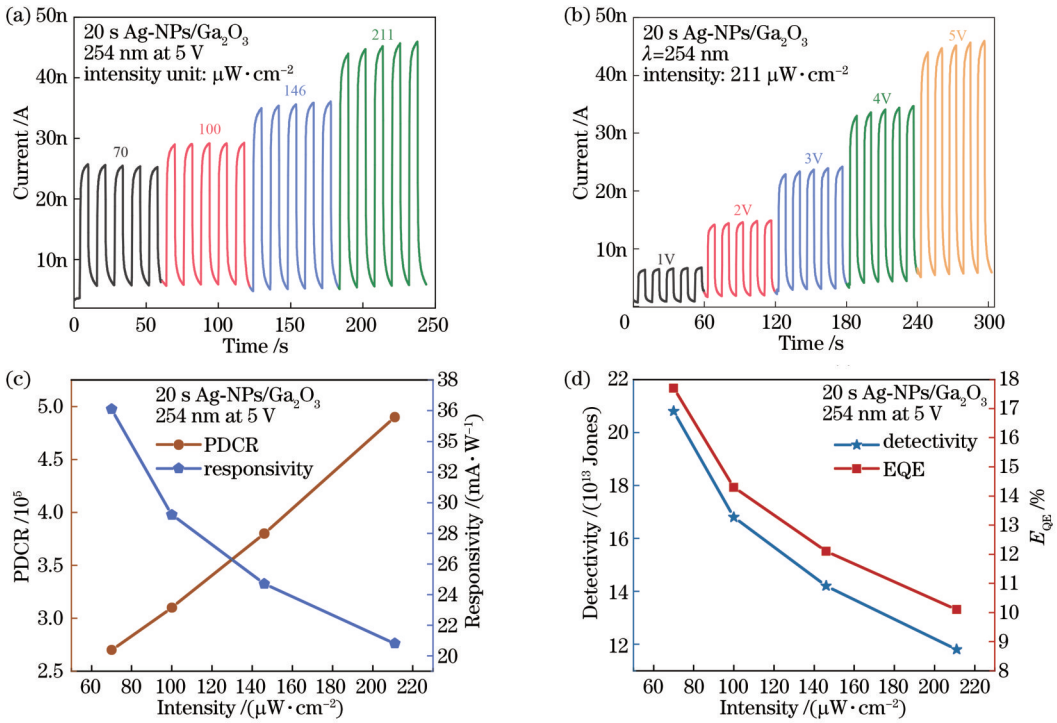

图 3 Ga_2O_3光电探测器的性能测试。(a)20 s Ag-NPs/Ga_2O_3薄膜光电探测器在 254 nm 紫外光照射下 5 V 偏压时不同光强的 *I-t* 曲线；(b)20 s Ag-NPs/Ga_2O_3薄膜光电探测器在 254 nm 紫外光照射下光强为 211 μW/cm^{2}时不同偏压下的 *I-t* 曲线；(c)PDCR 和光响应度与光强的线性关系曲线；(d)探测率和外量子效率与光强的线性关系曲线

Fig. 3 Performance test of Ga_2O_3 photodetectors. (a) *I-t* curve of 20 s Ag-NPs/Ga_2O_3 thin film photodetector under 254 nm UV irradiation at 5 V bias with different light intensities; (b) *I-t* curve of 20 s Ag-NPs/Ga_2O_3 thin film photodetector irradiated by 254 nm UV light with intensity of 211 μW/cm^2 under different bias voltages; (c) linear relationship curve of PDCR and responsivity with light intensity; (d) linear relationship curve of detectivity and E_{QE} with light intensity

测器会在高光强下发生自热效应。随着光强的增加，虽然会生成更多的光生载流子，但同时由于载流子散射和复合增强，很多光生载流子在被激发到导带前被重新复合，载流子输运效率下降，这就导致探测器的响应度随入射光强增大而减小[27]。探测器的探测率用 D^*表示，它是衡量探测器噪声性能的重要参数，是噪声等效功率(探测器可探测到的最小光信号的量值)的倒数，其定义式[28]为

$$D^* = \frac{R}{\sqrt{2qI_{dark}/S}}, \tag{4}$$

式中，q 为电子电荷。将式(3)中的 R 代入式(4)，可得 D^*为 2×10^{14} Jones。用 E_{QE}表示探测器的外量子效率，外量子效率是指被收集到的形成光电流的电子-空穴对数与入射光子数之比，其定义式[29]为

$$E_{QE} = \frac{hcR}{q\lambda} \times 100\%, \tag{5}$$

式中：h 为普朗克常量；c 为光速；λ 为入射光波长。将式(3)中的 R 代入式(5)，可得 E_{QE} 为 17.7%。由探测率和外量子效率的公式可得，该探测器的探测率和外量子效率与响应度 R 有关，也会随光强增加而减小，如图 3(d)所示。

为了研究光电探测器的瞬态响应表现，本文分别测试了非晶 Ga_2O_3和 Ag-NPs/Ga_2O_3探测器在电压为 5 V、波长为 254 nm 光照和黑暗状态下交替的瞬态反应，如图 4(a)～4(d)所示。为了定量分析，采用双指数公式对 *I-V* 特性曲线分别进行了拟合：

$$I = I_0 + A\exp(-t/\tau 1) + B\exp(-t/\tau 2), \tag{6}$$

式中：I_0 为稳定态的光电流；A、B 为常数；t 是打开和关闭的时间；τ_1 和 τ_2 为弛豫时间常数，图 4 中的 τ_r 和 τ_d 分别为上升沿和下降沿的两个常数[30]。从表 1 中可以看出，无论是非晶 Ga_2O_3探测器还是 Ag-NPs/Ga_2O_3探测器，都有着较短的响应时间。且 Ag 纳米颗粒的溅射对探测器的光谱响应时间没有明显的影响。

为了更好地比较 20 s Ag-NPs/Ga_2O_3薄膜光电探测器的性能，在表 2 中列出了一些相关参数。可以看出，20 s Ag-NPs/Ga_2O_3探测器较已报道的非晶 Ga_2O_3探测器表现出更低的暗电流，这可能是由于 Ag 纳米颗粒(功函数为 4.6 eV)与 Ga_2O_3(功函数为 4.16 eV)界面处能够形成肖特基接触，因此实现了更小的暗电流。紫外光照下，Ag 纳米颗粒的引入增强了 Ga_2O_3薄膜对紫外光更有效的吸收，且 Ag 纳米颗粒产生的大量热电子能够克服界面处的肖特基势垒产生更大的光电流，因此 Ag-NPs/Ga_2O_3薄膜的光暗电流比和探测率也稍高于其他一些非晶 Ga_2O_3薄膜基光电探测器。

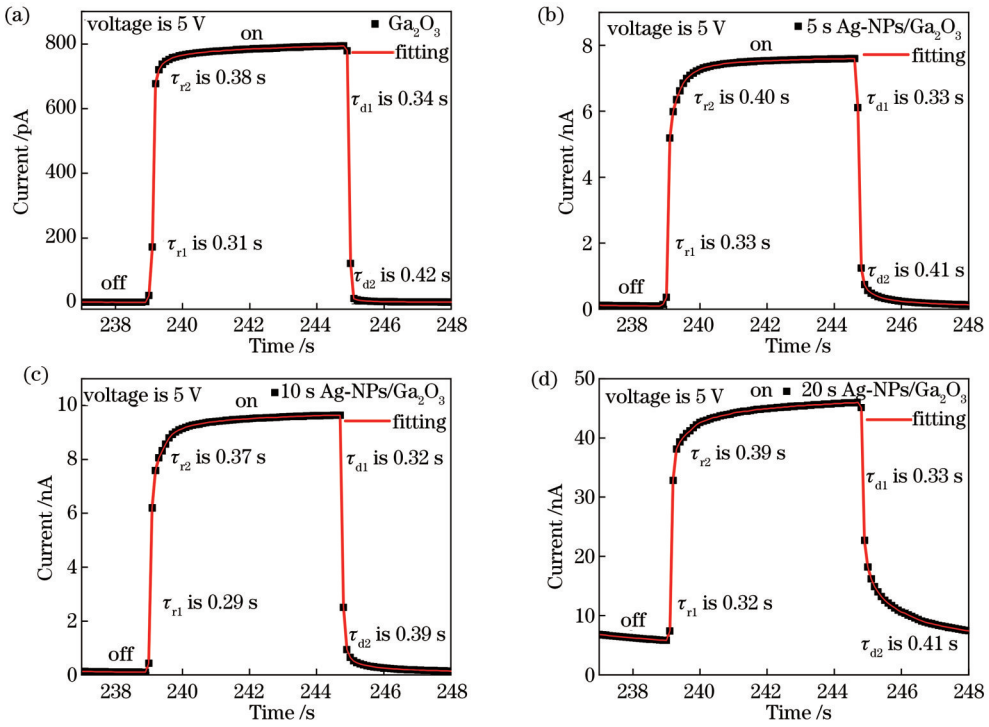

图 4 不同薄膜光电探测器的上升沿和下降沿的拟合曲线。(a)Ga_2O_3;(b)5 s Ag-NPs/Ga_2O_3;(c)10 s Ag-NPs/Ga_2O_3;(d)20 s Ag-NPs/Ga_2O_3

Fig. 4 Fitting curves of rising and falling edges of different thin film photodetectors. (a) Ga_2O_3; (b) 5 s Ag-NPs/Ga_2O_3; (c) 10 s Ag-NPs/Ga_2O_3; (d) 20 s Ag-NPs/Ga_2O_3

表 1 薄膜光电探测器的上升沿和下降沿时间常数

Table 1 Time constants of rising and falling edges of thin film photodetectors unit: s

Photodetector	τ_{r1}	τ_{r2}	τ_{d1}	τ_{d2}
Ga_2O_3	0.31	0.38	0.34	0.42
5 s Ag-NPs/Ga_2O_3	0.33	0.40	0.33	0.41
10 s Ag-NPs/Ga_2O_3	0.29	0.37	0.32	0.39
20 s Ag-NPs/Ga_2O_3	0.32	0.39	0.33	0.41

表 2 20 s Ag-NPs/Ga_2O_3薄膜光电探测器与其他最近报道的Ga_2O_3基光电探测器的性能对比

Table 2 Performance comparison of 20 s Ag-NPs/Ga_2O_3 thin film photodetector with other recently reported Ga_2O_3-based photodetectors

Photodetector	UV light /nm	I_{dark} /A	PDCR	R (A•W^{-1})	D^* /Jones	Reference
Al/Ga_2O_3	254	1.52×10^{-10}@20 V	2.55×10^{4}@20 V	0.8@20 V	1.1×10^{11}@20 V	[13]
Al/Ga_2O_3	254	~1.00×10^{-8}@15 V	~2.00×10^{3}@15 V	23.2@15 V	~2.0×10^{11}@15 V	[31]
Ga/Ga_2O_3	254	8.52×10^{-12}@10 V	~8.00×10^{5}@10 V	2.9@15 V	—	[32]
Amorphous Ga_2O_3	254	~2.00×10^{-7}@10 V	—	0.2@10 V	—	[19]
Amorphous Ga_2O_3	254	1.02×10^{-9}@10 V	—	3.2×10^{-3}@5 V	—	[33]
Amorphous Ga_2O_3	254	9.43×10^{-12}@10 V	—	1.3@10 V	—	[11]
Amorphous Ga_2O_3	250	2.32×10^{-10}@5 V	319.00@5 V	1.5@5 V	1.1×10^{14}@5 V	[34]
Ga_2O_3/CuI microwire	254	~8.50×10^{-15}@0 V	—	8.5×10^{-3}@0 V	7.8×10^{11}@0 V	[35]
PEDOTs/Ga_2O_3	254	~1.00×10^{-13}@−0.5 V	—	2.6@0 V	~1.0×10^{13}@−0.5 V	[36]
β-Ga_2O_3	254	1.10×10^{-10}@9 V	6.38×10^{5}@9 V	2.3@9 V	~5.5×10^{13}@9 V	[37]
20 s Ag-NPs/Ga_2O_3	254	9.40×10^{-14}@5 V	5.90×10^{5}@5 V	36.1×10^{-3}@5 V	2.0×10^{14}@5 V	This work
10 s Ag-NPs/Ga_2O_3	254	6.70×10^{-14}@5 V	6.70×10^{4}@5 V	6.0×10^{-3}@5 V	4.1×10^{12}@5 V	This work
5 s Ag-NPs/Ga_2O_3	254	1.10×10^{-13}@5 V	1.40×10^{5}@5 V	5.0×10^{-3}@5 V	2.7×10^{12}@5 V	This work

4 结 论

综上所述，在常温生长的非晶Ga_2O_3薄膜的基础上引入Ag纳米颗粒，成功制备了金属Ag纳米颗粒复合Ga_2O_3薄膜的日盲紫外光电探测器。该探测器表现出优异的探测性能，在5 V偏压下，探测器的暗电流低至94 fA，光暗电流比高达5.9×10^5，254 nm/365 nm波长抑制比达到1.6×10^4，响应度为36.1 mA/W，探测率为2×10^{14} Jones，外量子效率为17.7%。这不仅得益于紫外光下Ag纳米颗粒的等离子振动使得更多的入射光散射到Ga_2O_3薄膜层，从而提高了Ga_2O_3薄膜对光的吸收；而且Ag纳米颗粒在紫外光下可产生大量热载流子，使热电子有足够能量越过Ag纳米颗粒和Ga_2O_3薄膜形成的肖特基势垒，这两者都极大提高了探测器的光电流。此外，Ag纳米颗粒与Ga_2O_3薄膜间的肖特基势垒的形成有助于减小非晶Ga_2O_3的暗电流。本文工作意味着贵金属纳米颗粒的引入为实现低成本、低暗电流、高光暗电流比的日盲紫外探测器提供了一种可行的方案。

参 考 文 献

[1] 王丹，王晓丹，马海，等. Ga_2O_3材料的掺杂研究进展[J]. 激光与光电子学进展，2021，58(15): 1516025.
Wang D, Wang X D, Ma H, et al. Progress of doping in Ga_2O_3 materials[J]. Laser & Optoelectronics Progress, 2021, 58(15): 1516025.

[2] Chen X, Liu K W, Zhang Z Z, et al. Self-powered solar-blind photodetector with fast response based on Au/β-Ga_2O_3 nanowires array film Schottky junction[J]. ACS Applied Materials & Interfaces, 2016, 8(6): 4185-4191.

[3] 吴刚，唐利斌，郝群，等. 基于Pt/GaN/AlGaN异质结高响应度双波段紫外探测器[J]. 光学学报，2023，43(3): 0304002.
Wu G, Tang L B, Hao Q, et al. Dual-band and high-responsivity ultraviolet detector based on Pt/GaN/AlGaN heterojunction[J]. Acta Optica Sinica, 2023, 43(3): 0304002.

[4] Varshney U, Aggarwal N, Gupta G. Current advances in solar-blind photodetection technology: using Ga_2O_3 and AlGaN[J]. Journal of Materials Chemistry C, 2022, 10(5): 1573-1593.

[5] Hou Y N, Mei Z X, Du X L. Semiconductor ultraviolet photodetectors based on ZnO and $Mg_xZn_{1-x}O$[J]. Journal of Physics D: Applied Physics, 2014, 47(28): 283001.

[6] Fan M M, Liu K W, Zhang Z Z, et al. High-performance solar-blind ultraviolet photodetector based on mixed-phase ZnMgO thin film[J]. Applied Physics Letters, 2014, 105(1): 011117.

[7] Lu Y J, Lin C N, Shan C X. Optoelectronic diamond: growth, properties, and photodetection applications[J]. Advanced Optical Materials, 2018, 6(20): 1800359.

[8] Huang L, Feng Q, Han G Q, et al. Comparison study of β-Ga_2O_3 photodetectors grown on sapphire at different oxygen pressures[J]. IEEE Photonics Journal, 2017, 9(4): 1-8.

[9] Ji X Q, Yin X M, Yuan Y Z, et al. Amorphous Ga_2O_3 Schottky photodiodes with high-responsivity and photo-to-dark current ratio[J]. Journal of Alloys and Compounds, 2023, 933: 167735.

[10] 王尘，张宇超，范伟航，等. 氧气退火温度对室温脉冲激光沉积氧化镓薄膜特性的影响[J]. 光学学报，2022，42(8): 0831001.
Wang C, Zhang Y C, Fan W H, et al. Effect of oxygen annealing temperature on properties of Ga_2O_3 thin films grown at room temperature by pulsed laser deposition[J]. Acta Optica Sinica, 2022, 42(8): 0831001.

[11] Zhou C Q, Liu K W, Chen X, et al. Performance improvement of amorphous Ga_2O_3 ultraviolet photodetector by annealing under oxygen atmosphere[J]. Journal of Alloys and Compounds, 2020, 840: 155585.

[12] Heinemann M D, Berry J, Teeter G, et al. Oxygen deficiency and Sn doping of amorphous Ga_2O_3[J]. Applied Physics Letters, 2016, 108(2): 022107.

[13] 况丹，徐爽，史大为，等. 基于铝纳米颗粒修饰的非晶氧化镓薄膜日盲紫外探测器[J]. 物理学报，2023，72(3): 038501.
Kuang D, Xu S A, Shi D W, et al. High performance amorphous Ga_2O_3 thin film solar blind ultraviolet photodetectors decorated with Al nanoparticles[J]. Acta Physica Sinica, 2023, 72(3): 038501.

[14] Zhao Z Q, Chu C S, Zhang G, et al. Tuning the plasmonic resonance peak for Al nanorods on AlGaN layer to deep ultraviolet band[J]. IEEE Photonics Journal, 2021, 13(5): 4800107.

[15] 石雄林，刘宏宇，候爽，等. 表面等离子体在氧化镓基紫外探测器中的应用[J]. 光电工程，2018，45(2): 85-92.
Shi X L, Liu H Y, Hou S, et al. The applications of surface plasmons in Ga_2O_3 ultraviolet photodetector[J]. Opto-Electronic Engineering, 2018, 45(2): 85-92.

[16] An Y H, Chu X L, Huang Y Q, et al. Au plasmon enhanced high performance β-Ga_2O_3 solar-blind photo-detector[J]. Progress in Natural Science: Materials International, 2016, 26(1): 65-68.

[17] Wang S L, Wu C, Wu F M, et al. Flexible, transparent and self-powered deep ultraviolet photodetector based on Ag NWs/amorphous gallium oxide Schottky junction for wearable devices[J]. Sensors and Actuators A: Physical, 2021, 330: 112870.

[18] Asanithi P, Chaiyakun S, Limsuwan P. Growth of silver nanoparticles by DC magnetron sputtering[J]. Journal of Nanomaterials, 2012, 2012: 1-8.

[19] Cui S J, Mei Z X, Zhang Y H, et al. Room-temperature fabricated amorphous Ga_2O_3 high-response-speed solar-blind photodetector on rigid and flexible substrates[J]. Advanced Optical Materials, 2017, 5(19): 1700454.

[20] Xu Y, An Z Y, Zhang L X, et al. Solar blind deep ultraviolet β-Ga_2O_3 photodetectors grown on sapphire by the Mist-CVD method[J]. Optical Materials Express, 2018, 8(9): 2941-2947.

[21] Qin Y, Long S B, He Q M, et al. Amorphous gallium oxide-based gate-tunable high-performance thin film phototransistor for solar-blind imaging[J]. Advanced Electronic Materials, 2019, 5(7): 1900389.

[22] Han S, Huang X L, Fang M Z, et al. High-performance UV detectors based on room-temperature deposited amorphous Ga_2O_3 thin films by RF magnetron sputtering[J]. Journal of Materials Chemistry C, 2019, 7(38): 11834-11844.

[23] Liu Z, Zhi Y S, Li S, et al. Comparison of optoelectrical characteristics between Schottky and Ohmic contacts to β-Ga_2O_3 thin film[J]. Journal of Physics D: Applied Physics, 2020, 53(8): 085105.

[24] Dong L P, Pang T Q, Yu J G, et al. Performance-enhanced solar-blind photodetector based on a $CH_3NH_3PbI_3$/β-Ga_2O_3 hybrid structure[J]. Journal of Materials Chemistry C, 2019, 7(45): 14205-14211.

[25] Peng Y K, Zhang Y, Chen Z W, et al. Arrays of solar-blind ultraviolet photodetector based on β-Ga_2O_3 epitaxial thin films[J]. IEEE Photonics Technology Letters, 2018, 30(11): 993-996.

[26] Wang Y H, Cui W J, Yu J, et al. One-step growth of amorphous/crystalline Ga_2O_3 phase junctions for high-performance solar-blind photodetection[J]. ACS Applied Materials & Interfaces, 2019, 11(49): 45922-45929.

[27] Li S, Yue J Y, Wu C, et al. Self-powered ultraviolet photodetector based on β-Ga_2O_3/WO_3 NPs heterojunction with low noise and high visible rejection[J]. IEEE Sensors Journal,

2021, 21(23): 26724-26730.

[28] Zhang Y F, Chen X H, Xu Y, et al. Transition of photoconductive and photovoltaic operation modes in amorphous Ga_2O_3-based solar-blind detectors tuned by oxygen vacancies[J]. Chinese Physics B, 2019, 28(2): 028501.

[29] Wang Y H, Li H R, Cao J, et al. Ultrahigh gain solar blind avalanche photodetector using an amorphous Ga_2O_3-based heterojunction[J]. ACS Nano, 2021, 15(10): 16654-16663.

[30] Kumar N, Arora K, Kumar M. High performance, flexible and room temperature grown amorphous Ga_2O_3 solar-blind photodetector with amorphous indium-zinc-oxide transparent conducting electrodes[J]. Journal of Physics D: Applied Physics, 2019, 52(33): 335103.

[31] Yu J G, Li Q A, Yao H Z, et al. The performance of Al plasmon enhanced β-Ga_2O_3 solar-blind photodetector[J]. Scientia Sinica Physica, Mechanica & Astronomica, 2022, 52(9): 297305.

[32] Cui S J, Mei Z X, Hou Y N, et al. Enhanced photoresponse performance in Ga/Ga_2O_3 nanocomposite solar-blind ultraviolet photodetectors[J]. Chinese Physics B, 2018, 27(6): 067301.

[33] Guo D Y, Zhao X L, Zhi Y S, et al. Epitaxial growth and solar-blind photoelectric properties of corundum-structured α-Ga_2O_3 thin films[J]. Materials Letters, 2016, 164: 364-367.

[34] Zhu W H, Xiong L X, Si J W, et al. Influence of deposition temperature on amorphous Ga_2O_3 solar-blind ultraviolet photodetector[J]. Semiconductor Science and Technology, 2020, 35(5): 055037.

[35] Li S, Zhi Y S, Lu C, et al. Broadband ultraviolet self-powered photodetector constructed on exfoliated β-Ga_2O_3/CuI core-shell microwire heterojunction with superior reliability[J]. The Journal of Physical Chemistry Letters, 2021, 12(1): 447-453.

[36] Wang H B, Chen H Y, Li L, et al. High responsivity and high rejection ratio of self-powered solar-blind ultraviolet photodetector based on PEDOT: PSS/β-Ga_2O_3 organic/inorganic p-n junction[J]. The Journal of Physical Chemistry Letters, 2019, 10(21): 6850-6856.

[37] Vieira D H, Badiei N, Evans J E, et al. Improvement of the deep UV sensor performance of a β-Ga_2O_3 photodiode by coupling of two planar diodes[J]. IEEE Transactions on Electron Devices, 2020, 67(11): 4947-4952.

Preparation and Study of Ag Nanoparticles Composite Amorphous Gallium Oxide Photodetector

Xu Qiang, Yang Lili**, Liu Zeng, Zhang Maolin, Li Shan, Tang Weihua*

College of Integrated Circuit Science and Engineering, Nanjing University of Posts and Telecommunications, Nanjing 210023, *Jiangsu, China*

Abstract

Objective Thanks to the low false alarm rate and high signal-to-noise ratio, deep ultraviolet (DUV) photodetector (PD) shows great application potential in ozone hole detection, high-voltage electric fire alarm, stealth bomber, and missile alarm. Gallium oxide (Ga_2O_3) is one of the most ideal materials for DUV PDs due to its suitable and tunable bandgap (4.5-5.3 eV), simple preparation process, and high stability. Nowadays, many studies focused on crystalline Ga_2O_3 film DUV PDs, but the lattice mismatch and strict growth parameters during the preparation put forward higher requirements for substrate materials and growth equipment. Compared with crystalline Ga_2O_3, amorphous Ga_2O_3 films have low preparation requirements and are easier to generate larger photocurrents due to the promotion of carrier separation by intrinsic defects. However, amorphous Ga_2O_3 is prone to higher dark current due to more defects. It is necessary to introduce noble metal Ag nanoparticles (Ag-NPs) to improve the photodetection performance of amorphous Ga_2O_3. On one hand, the formation of Schottky barriers between Ag-NPs and Ga_2O_3 films helps reduce the dark current of amorphous Ga_2O_3. On the other hand, the surface plasmon vibration of Ag-NPs can enhance the absorption of Ga_2O_3 to UV light. Additionally, Ag-NPs can generate a large number of hot carriers under UV light to allow hot electrons with sufficient energy to overcome the Schottky barriers. We provide a feasible approach to realize DUV PDs with low dark current and high photo-to-dark current ratio (PDCR).

Methods Amorphous Ga_2O_3 films are grown on sapphire substrates by the facile radio frequency (RF) magnetron sputtering technology. The sputtering is carried out at room temperature for 70 min with chamber pressure and Argon flow rate of 1 Pa and 20 sccm respectively. The obtained Ga_2O_3 films are cut into four parts, and three of them are continuously sputtered with Ag-NPs on the Ga_2O_3 surface by direct-current (DC) magnetron sputtering. The sputtering time is 5, 10, and 20 s respectively. The obtained samples are labeled as 5 s Ag-NPs/Ga_2O_3, 10 s Ag-NPs/Ga_2O_3, and 20 s Ag-NPs/Ga_2O_3. Finally, the four samples obtained previously are annealed in a tube furnace for 2 h at an annealing temperature of 200 °C. The crystal structure of the sample is characterized by X-ray diffractometer (XRD), the cross-section morphology of the sample is by scanning electron microscope (SEM), and the surface morphology of the sample is by atomic force microscope (AFM). Additionally, the absorption spectrum features Q6 ultraviolet-visible (UV-Vis) spectrophotometer, and the low-pressure mercury lamps with wavelengths of 254 nm and 365 nm are employed as the ultraviolet light source.

A pair of cylindrical metal indium (In) with a diameter of 1 mm and a spacing of 1 mm is pressed on the surface of samples as electrodes, and the current-voltage (*I-V*) characteristics and transient response curve (*I-t*) of the PDs are measured by a B1505A power device analyzer.

Results and Discussions AFM results confirm the introduction of Ag-NPs on the surface of amorphous Ga_2O_3 films, and the surface mean square root (RMS) roughness of the Ag-NPs/Ga_2O_3 film after sputtering Ag nanoparticles for 20 s is significantly increased from 0.218 to 6.390 nm [Figs. 1 (c) and 1(d)]. Meanwhile, the absorption of Ga_2O_3 to UV light also increases obviously after sputtering Ag-NPs [Fig. 1 (e)]. 20 s Ag-NPs/Ga_2O_3 presents a lower dark current than amorphous Ga_2O_3 due to the Schottky junction formed between Ag-NPs and Ga_2O_3 films, which further forms a potential barrier and reduces the dark current [Fig. 2 (a)]. Under the irradiation of 254 nm UV light, Ag-NPs/Ga_2O_3 films exhibit a higher photocurrent than amorphous Ga_2O_3. In particular, the photocurrent of 20 s Ag-NPs/Ga_2O_3 at 5 V is 18.8 times higher than that of amorphous Ga_2O_3[Fig. 2 (b)]. This may be due to the enhanced scattering of UV light by the plasmonic vibrations of the Ag-NPs on the surface of Ga_2O_3 films, thus leading to enhanced absorption of UV light by Ga_2O_3 and an increase in the photocurrent of the Ag-NPs/Ga_2O_3 PD. Additionally, the Ag-NPs vibration may generate a large number of hot carriers to have enough energy to cross the Schottky barriers between Ag-NPs and Ga_2O_3 films, which leads to an increase in the photocurrent of the PD. At this point, the PDCR is as high as 5.9×10^5, the rejection ratio (254 nm/365 nm) is 1.6×10^4[Fig. 2 (c)], and the responsivity is 36.1 mA/W [Fig. 3 (c)], with the detectivity of 2×10^{14} Jones and external quantum efficiency of 17.7% [Fig. 3 (d)]. Meanwhile, both the amorphous Ga_2O_3 detector and the Ag-NPs/Ga_2O_3 detector have short response time (Fig. 4).

Conclusions In summary, the Ag-NP composite amorphous Ga_2O_3 film DUV PD is prepared by a room temperature magnetron sputtering technology. The PD exhibits an excellent photodetection performance. Under 5 V voltage, the dark current of the detector is as low as 94 fA and the PDCR is as high as 5.9×10^5, and the rejection ratio (254 nm/365 nm) is 1.6×10^4, with the responsivity of 36.1 mA/W, detectivity of 2×10^{14} Jones, and external quantum efficiency of 17.7%. This is not only attributed to the plasmonic vibration of Ag-NPs under UV light, which scatters more incident light into the Ga_2O_3 film layer to enhance the UV light absorption of the Ga_2O_3 films, but also to the generation of a large number of hot carriers by Ag-NPs under UV light. These hot carriers enable the hot electrons to overcome the Schottky barriers formed by Ag-NPs and Ga_2O_3 films, which brings about a significant increase in the PD photocurrent. In addition, the formation of the Schottky barriers between Ag-NPs and Ga_2O_3 films helps reduce the dark current in the amorphous Ga_2O_3. This study implies that the introduction of noble metal nanoparticles provides a viable solution to DUV PDs with low cost, dark current, and high PDCR.

Key words photodetector; gallium oxide; Ag nanoparticles; hot electron; Schottky barrier